Analysis of Vibration Characteristics of Electro-hydraulic 3-UPS/S Parallel Stabilized Platform

xiaoming yuan (xiaomingbingbing@163.com)
Yanshan University https://orcid.org/0000-0001-5779-1366
Weiqi Wang
Yanshan University
Haodong Pang
Yanshan University
Lijie Zhang
Yanshan University

Research Article

Keywords: Electro-hydraulic driven 3-UPS/S parallel stabilized platform, Kinetic equation, Vibration mode, Vibration response, Modal test

Posted Date: April 27th, 2023

DOI: https://doi.org/10.21203/rs.3.rs-2730927/v1

ORIGINAL ARTICLE

Analysis of Vibration Characteristics of Electro-hydraulic Driven 3-UPS/S Parallel Stabilized Platform

Xiaoming Yuan[1,2,*], Weiqi Wang[1,2], Haodong Pang[1,2], Lijie Zhang[1,2]

Abstract

With the development of fluid power transmission and control and control technology, using electro-hydraulic driven can significantly improve the load-carrying capacity, stiffness, and control accuracy of the stabilization platforms. However, compared to mechanical driven, electro-hydraulic driven parallel stabilization platform needs to consider the stiffness and damping of the fluid, as well as the coupling effect between the fluid and the structure, making the modal and dynamic response characteristics of the mechanism more complex. Aiming at the above problems, taking the electro-hydraulic driven 3-UPS/S parallel stable platform as the research object, considering the hinge stiffness, the vibration characteristic equation of the mechanism was established by using the virtual work principle. Then the variation characteristics of natural frequency and vibration response with the position of mechanism were analyzed basing on the dynamic equation. Finally, the correctness of the model was verified by modal test and Runge-Kutta methods. This study can provide a theoretical basis for the dynamic design of electro-hydraulic driven parallel mechanisms.

Keywords: Electro-hydraulic driven 3-UPS/S parallel stabilized platform, Kinetic equation, Vibration mode, Vibration response, Modal test

1 Introduction

The stabilized platform detects the posture change of the equipment through the sensitive element, compensates the deviation of the equipment through attitude adjustment, and isolates the influence of the environment to keep the equipment relatively stable in the inertial space [1-4]. According to the mechanism type, the mechanism can be classified into series stabilized platform and parallel stabilized platform [5-6]. The series stabilized platform is simple in control and low in design cost. Thus, it is widely used in fields like laser positioning, satellite communication, missile guidance and unmanned reconnaissance aircraft. Because of its characteristics of strong bearing capacity, high stiffness and easy multi-axis coupling driven, the parallel stabilized platform has a wide range of application scenarios in high-precision operations such as weapon launch and maritime rescue [7-10]. By adopting the electro-hydraulic driven with the advantages of high power/weight ratio, fast response speed and small cumulative error, the motion control accuracy of the stabilized platform is greatly improved [11-12].

To further improve the performance of parallel stabilized platform, it is important to study its vibration characteristics [13-14]. There are three methods to study the vibration characteristics: simulation analysis method [15-17], theoretical analysis method [18] and experimental analysis method [19]. The simulation analysis method is to analyze the vibration characteristics after solving the characteristic value of the finite element analysis of the structure [20-22]. Therefore, it is widely used in analyzing vibration characteristics of complex mechanical systems. The experimental analysis method is to estimate the modal parameters of the mechanism through the frequency response function measured in practice and used to verify the conclusion of simulation and theoretical analysis [23-24]. Theoretical analysis method is to analyze the vibration characteristics based on the dynamic equation and the analytical solution of vibration response [25-26]. It can quantitatively analyze the vibration characteristics of mechanism, and it is a common method for further study of mechanical vibration. However, during the process of dynamic modeling, the influence of hinges stiffness is usually ignored, and the variation characteristics of natural frequency and vibration response with the position of

*Correspondence: xiaomingbingbing@163.com
[1] Hebei Key Laboratory of Heavy Machinery Fluid Power Transmission and Control, Yanshan University, Qinhuangdao, 066004

mechanism have not been studied yet.

Therefore, taking the electro-hydraulic driven 3-UPS/S parallel stabilized platform as the research object, the mechanical-hydraulic coupling dynamic equation is established considering the hinge stiffness. Then, the modal characteristics and resonant characteristics of the mechanism are studied. The theoretical model is verified by numerical simulation and modal test. This study can provide a theoretical basis for the dynamic modal analysis and resonance research of parallel mechanism.

2 Kinematic analysis of Electro-Hydraulic Driven 3-UPS/S Parallel Stabilized Platform

2.1 Position Analysis of Electro-hydraulic Driven 3-UPS/S Parallel Stabilized Platform

As shown in Figure 1a), the electro-hydraulic driven 3-UPS/S parallel stabilized platform consists of a moving platform, a supporting branch chain, a static platform, and three driving branches. Coordinate system *U-xyz* is the fixed coordinate system of the moving platform and coordinate system *D-XYZ* is the fixed coordinate system of the static platform.

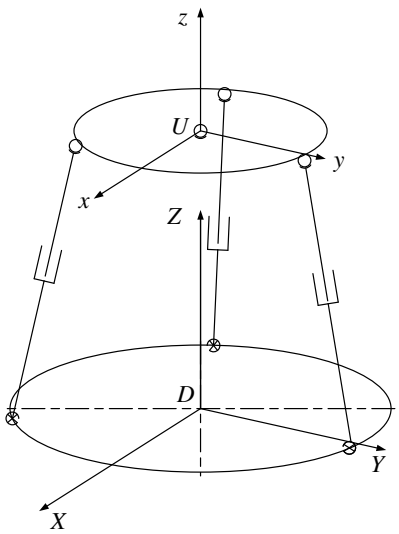

a) Schematic diagram of electro-hydraulic driven 3-UPS/S parallel stabilized platform

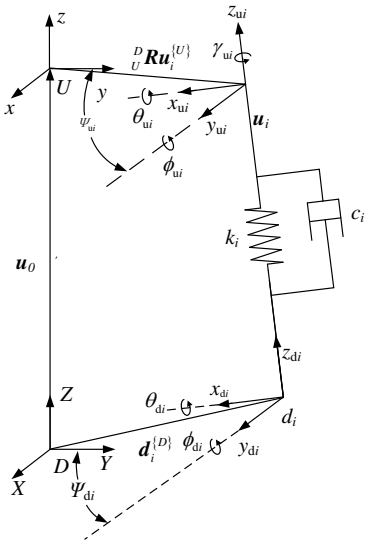

b) Drive chain position vector diagram

Figure 1 Coordinate system of electro-hydraulic 3-UPS/S parallel stabilized platform

As shown in Figure 1b), the local coordinate system d_i-$x_{di}y_{di}z_{di}$ is established at the center of the universal joint, and the local coordinate system u_i-$x_{ui}y_{ui}z_{ui}$ is established at the center of the spherical hinge. Axis z_{di} and axis z_{ui} are in the same direction as the unit direction vector $\boldsymbol{e}_i$ of the driving branch. The rotation angle of the universal joint about axis x_{di} and axis y_{di} are respectively θ_{di} and ϕ_{di}; the rotation angle of the spherical hinge about axis x_{ui}, axis y_{ui} and axis z_{ui} are respectively θ_{ui}, ϕ_{ui}, γ_{ui}; ψ_{di}, ψ_{ui} are respectively the installation angles of universal joint and spherical hinge, which are determined by the platform structure.

The closed-loop equation of the drive chain can be expressed as:

$$l_i\boldsymbol{e}_i = {}^{D}_{U}\boldsymbol{R}\boldsymbol{u}_i^{\{U\}} - \boldsymbol{d}_i^{\{D\}} + \boldsymbol{u}_0 + \boldsymbol{u}\,, \tag{1}$$

Where l_i is the length of the drive chain; $\boldsymbol{e}_i$ is the unit direction vector of the drive chain; ${}^{D}_{U}\boldsymbol{R}$ is the rotation transformation matrix between coordinate system *U-xyz* and coordinate system *D-XYZ*; $\boldsymbol{u}_i^{\{U\}}$ is the vector from the center of spherical hinge to the origin of coordinate system *U-xyz*; $\boldsymbol{d}_i^{\{D\}}$ is the vector from the center of universal joint to the origin of coordinate system *D-XYZ*; $\boldsymbol{u}_0$ is the initial displacement vector of coordinate system *U-xyz* to coordinate system *D-XYZ*; $\boldsymbol{u}$ is the displacement vector of coordinate system *U-xyz* to coordinate system *D-XYZ*.

Thus, the expression of the drive chain length can be expressed as:

$$l_i = \left\| {}^{D}_{U}\boldsymbol{R}\boldsymbol{u}_i^{\{U\}} - \boldsymbol{d}_i^{\{D\}} + \boldsymbol{u}_0 + \boldsymbol{u} \right\|, \tag{2}$$

The centroid position of the lower connecting rod of the drive chain can be expressed as:

$$\boldsymbol{p}_{gi} = \boldsymbol{d}_i^{\{D\}} + q_i \boldsymbol{e}_i, \tag{3}$$

Where $\boldsymbol{p}_{gi}$ is the position vector of the lower connecting rod centroid; q_i is the distance between the centroid of the lower connecting rod and the center of universal joint.

The rotation transformation matrix between local coordinate system d_i-$x_{di}y_{di}z_{di}$ and coordinate system D-XYZ can be expressed as:

$${}^{D}_{d_i}\boldsymbol{R} = \boldsymbol{R}(z_{di}, \psi_{di})\boldsymbol{R}(y_{di}, \phi_{di})\boldsymbol{R}(x_{di}, \theta_{di}), \tag{4}$$

Since axis z_{di} is in the same direction as the unit direction vector $\boldsymbol{e}_i$, then z_{di} can be expressed as:

$$\begin{bmatrix} e_{ix} \\ e_{iy} \\ e_{iz} \end{bmatrix} = \begin{bmatrix} \sin\psi_{di}\sin\theta_{di} + \cos\psi_{di}\sin\phi_{di}\cos\theta_{di} \\ \sin\psi_{di}\sin\phi_{di}\cos\theta_{di} - \cos\psi_{di}\cos\theta_{di} \\ \cos\phi_{di}\cos\theta_{di} \end{bmatrix}, \tag{5}$$

Thus, the rotation angle of the universal joint is:

$$\begin{cases} \phi_{di} = \arctan\left(\dfrac{e_{ix}\cos\psi_{di} + e_{iy}\sin\psi_{di}}{e_{iz}}\right) \\ \theta_{di} = -\arcsin(e_{iy}\cos\psi_{di} - e_{ix}\sin\psi_{di}) \end{cases}, \tag{6}$$

If local coordinate system d_i-$x_{di}y_{di}z_{di}$ and u_i-$x_{ui}y_{ui}z_{ui}$ have the same direction, the rotation transformation matrix ${}^{D}_{u_i}\boldsymbol{R}$ between local coordinate system u_i-$x_{ui}y_{ui}z_{ui}$ and coordinate system D-XYZ can be obtained from Eq. (4). Thus, the rotation angle of the spherical hinge is:

$$\begin{cases} \phi_{ui} = \arctan\left(\dfrac{(\boldsymbol{R}_{Fi})_{1,3}}{(\boldsymbol{R}_{Fi})_{3,3}}\right) \\ \theta_{ui} = -\arcsin((\boldsymbol{R}_{Fi})_{2,3}) \\ \gamma_{ui} = \arctan\left(\dfrac{(\boldsymbol{R}_{Fi})_{2,1}}{(\boldsymbol{R}_{Fi})_{2,2}}\right) \end{cases}, \tag{7}$$

Where $\boldsymbol{R}_{Fi} = \boldsymbol{R}(z_{ui}, \psi_{ui})^{T}{}^{D}_{U}\boldsymbol{R}^{T}\,{}^{D}_{u_i}\boldsymbol{R}^{T}$.

2.2 Velocity Analysis of Electro-hydraulic Driven 3-UPS/S Parallel Stabilized Platform

By solving the first derivative of time of Eq. (1), the velocity equation of the drive chain can be expressed as:

$$\dot{l}_i\boldsymbol{e}_i + l_i\boldsymbol{\omega}_{zi} \times \boldsymbol{e}_i = \boldsymbol{\omega}_u \times {}^{U}_{D}\boldsymbol{R}\boldsymbol{u}_i^{\{U\}}, \tag{8}$$

Where $\boldsymbol{\omega}_{zi}$ is the angular velocity of drive chain; $\boldsymbol{\omega}_u$ is the angular velocity of moving platform.

Then the Jacobian matrix between the drive chain and the moving platform is:

$$\boldsymbol{J}_u = \begin{bmatrix} {}^{U}_{D}\boldsymbol{R}\boldsymbol{u}_1^{\{U\}} \times \boldsymbol{e}_1 \\ {}^{U}_{D}\boldsymbol{R}\boldsymbol{u}_2^{\{U\}} \times \boldsymbol{e}_2 \\ {}^{U}_{D}\boldsymbol{R}\boldsymbol{u}_3^{\{U\}} \times \boldsymbol{e}_3 \end{bmatrix}, \tag{9}$$

Multiplying both sides of Eq. (8) by the unit direction vector $\boldsymbol{e}_i$, and express the result in local coordinate system d_i-$x_{di}y_{di}z_{di}$, the result is shown as follows:

$$\begin{bmatrix} \left(\omega_z^{\{d_i\}}\right)_x \\ \left(\omega_z^{\{d_i\}}\right)_y \\ 0 \end{bmatrix} = \frac{1}{l_i}\begin{bmatrix} -\left(v_{ui}^{\{d_i\}}\right)_y \\ \left(v_{ui}^{\{d_i\}}\right)_x \\ 0 \end{bmatrix}, \tag{10}$$

Where $v_{ui}^{\{d_i\}}$ represents the center velocity of the spherical hinge in local coordinate system d_i-$x_{di}y_{di}z_{di}$.

The angular velocity of the drive chain is generated by the rotation of the universal joint, so the angular velocity of the drive chain rotation can be expressed in the local coordinate system d_i-$x_{di}y_{di}z_{di}$ as:

$$\omega_z = \dot{\phi}_{di}\boldsymbol{y}_{di} + \dot{\psi}_{di}\boldsymbol{x}_{di}, \tag{11}$$

By representing the vector in Eq. (9) in local coordinate system d_i-$x_{di}y_{di}z_{di}$, then Eq. (9) can be expressed as:

$$\begin{aligned} \boldsymbol{\omega}_z^{\{d_i\}} &= \dot{\phi}_{di}\boldsymbol{R}(\theta_{di}, x_{di})^{T}\boldsymbol{R}(\phi_{di}, y_{di})^{T}(0 \quad 1 \quad 0)^{T} \\ &\quad + \dot{\theta}_{di}\boldsymbol{R}(\theta_{di}, x_{di})^{T}(1 \quad 0 \quad 0)^{T} \\ &\approx (\dot{\theta}_{di} \quad \dot{\phi}_{di} \quad 0)^{T} \end{aligned}, \tag{12}$$

By combining Eqs. (10)-(12), the angular velocity of

universal joint can be expressed as:

$$\begin{cases} \dot{\phi}_{\mathrm{d}i} = -\dfrac{1}{l_i}\left({}^{d_i}_{U}\boldsymbol{R}\right)_{:,2}\left(\boldsymbol{\omega}_{\mathrm{u}} \times {}^{U}_{D}\boldsymbol{R}\boldsymbol{u}_i^{\{U\}}\right) \\ \dot{\theta}_{\mathrm{d}i} = \dfrac{1}{l_i}\left({}^{d_i}_{U}\boldsymbol{R}\right)_{:,1}\left(\boldsymbol{\omega}_{\mathrm{u}} \times {}^{U}_{D}\boldsymbol{R}\boldsymbol{u}_i^{\{U\}}\right) \end{cases}, \tag{13}$$

Then the Jacobian matrix of universal joint is:

$$\boldsymbol{J}_{\mathrm{fd}} = \begin{bmatrix} -\dfrac{1}{l_1}\left({}^{d_1}_{U}\boldsymbol{R}\right)_{:,2}\left(\boldsymbol{\omega}_{\mathrm{u}} \times {}^{U}_{D}\boldsymbol{R}\boldsymbol{u}_1^{\{U\}}\right) \\ -\dfrac{1}{l_2}\left({}^{d_2}_{U}\boldsymbol{R}\right)_{:,2}\left(\boldsymbol{\omega}_{\mathrm{u}} \times {}^{U}_{D}\boldsymbol{R}\boldsymbol{u}_2^{\{U\}}\right) \\ -\dfrac{1}{l_3}\left({}^{d_3}_{U}\boldsymbol{R}\right)_{:,2}\left(\boldsymbol{\omega}_{\mathrm{u}} \times {}^{U}_{D}\boldsymbol{R}\boldsymbol{u}_3^{\{U\}}\right) \end{bmatrix}, \tag{14}$$

$$\boldsymbol{J}_{\mathrm{xd}} = \begin{bmatrix} \dfrac{1}{l_1}\left({}^{d_1}_{U}\boldsymbol{R}\right)_{:,2}\left(\boldsymbol{\omega}_{\mathrm{u}} \times {}^{U}_{D}\boldsymbol{R}\boldsymbol{u}_1^{\{U\}}\right) \\ \dfrac{1}{l_2}\left({}^{d_2}_{U}\boldsymbol{R}\right)_{:,2}\left(\boldsymbol{\omega}_{\mathrm{u}} \times {}^{U}_{D}\boldsymbol{R}\boldsymbol{u}_2^{\{U\}}\right) \\ \dfrac{1}{l_3}\left({}^{d_3}_{U}\boldsymbol{R}\right)_{:,2}\left(\boldsymbol{\omega}_{\mathrm{u}} \times {}^{U}_{D}\boldsymbol{R}\boldsymbol{u}_3^{\{U\}}\right) \end{bmatrix}, \tag{15}$$

Similarly, considering the motion transmission relationship between the spherical hinge and the moving platform, the angular velocity of the drive chain can be expressed as:

$$\boldsymbol{\omega}_z = \boldsymbol{\omega}_{\mathrm{u}} + \dot{\phi}_{\mathrm{u}i}\boldsymbol{y}_{\mathrm{d}i} + \dot{\theta}_{\mathrm{u}i}\boldsymbol{x}_{\mathrm{u}i} + \dot{\gamma}_{\mathrm{u}i}\boldsymbol{z}_{\mathrm{u}i}, \tag{16}$$

By representing the vector in Eq. (14) in local coordinate system u_i-$x_{\mathrm{u}i}y_{\mathrm{u}i}z_{\mathrm{u}i}$, then Eq. (14) can be expressed as:

$$\begin{aligned} \boldsymbol{\omega}_{\mathrm{z}}^{\{u_i\}} &= \boldsymbol{\omega}_{\mathrm{u}}^{\{u_i\}} + \dot{\gamma}_{\mathrm{u}i}\boldsymbol{R}\left(z_{\mathrm{u}i}, \gamma_{\mathrm{u}i}\right)^{\mathrm{T}}\begin{pmatrix}0 & 0 & 1\end{pmatrix}^{\mathrm{T}} \\ &+\dot{\phi}_{\mathrm{u}i}\boldsymbol{R}\left(z_{\mathrm{u}i}, \gamma_{\mathrm{u}i}\right)^{\mathrm{T}}\boldsymbol{R}\left(x_{\mathrm{u}i}, \theta_{\mathrm{u}i}\right)^{\mathrm{T}}\boldsymbol{R}\left(y_{\mathrm{u}i}, \phi_{\mathrm{u}i}\right)^{\mathrm{T}}\begin{pmatrix}0 & 1 & 0\end{pmatrix}^{\mathrm{T}} \\ &+\dot{\theta}_{\mathrm{u}i}\boldsymbol{R}\left(z_{\mathrm{u}i}, \gamma_{\mathrm{u}i}\right)^{\mathrm{T}}\boldsymbol{R}\left(x_{\mathrm{u}i}, \theta_{\mathrm{u}i}\right)^{\mathrm{T}}\begin{pmatrix}1 & 0 & 0\end{pmatrix}^{\mathrm{T}} \\ &\approx \boldsymbol{\omega}_{\mathrm{u}}^{\{u_i\}} + \begin{pmatrix}\dot{\phi}_{\mathrm{u}i} & \dot{\theta}_{\mathrm{u}i} & \dot{\gamma}_{\mathrm{u}i}\end{pmatrix}^{\mathrm{T}} \end{aligned}, \tag{17}$$

By combining Eq. (11) and Eq. (17), the angular velocity of spherical hinge can be expressed as:

$$\begin{cases} \dot{\phi}_{\mathrm{u}i} = -\dfrac{1}{l_i}\left({}^{d_i}_{U}\boldsymbol{R}\right)_{:,2}\left(\boldsymbol{\omega}_{\mathrm{u}} \times {}^{U}_{D}\boldsymbol{R}\boldsymbol{u}_i^{\{U\}}\right) - \left({}^{D}_{u_i}\boldsymbol{R}\right)_{:,1}\boldsymbol{\omega}_{\mathrm{u}} \\ \dot{\theta}_{\mathrm{u}i} = \dfrac{1}{l_i}\left({}^{d_i}_{U}\boldsymbol{R}\right)_{:,1}\left(\boldsymbol{\omega}_{\mathrm{u}} \times {}^{U}_{D}\boldsymbol{R}\boldsymbol{u}_i^{\{U\}}\right) - \left({}^{D}_{u_i}\boldsymbol{R}\right)_{:,2}\boldsymbol{\omega}_{\mathrm{u}} \\ \dot{\gamma}_{\mathrm{u}i} = \dfrac{1}{l_i}\left({}^{d_i}_{U}\boldsymbol{R}\right)_{:,3}\boldsymbol{\omega}_{\mathrm{u}} \end{cases}, \tag{18}$$

Thus, the Jacobian matrix of spherical hinge can be expressed as:

$$\boldsymbol{J}_{\mathrm{gu}} = \begin{bmatrix} -\left({}^{D}_{u_i}\boldsymbol{R}\right)_{:,3}^{\mathrm{T}} \\ -\left({}^{D}_{u_i}\boldsymbol{R}\right)_{:,3}^{\mathrm{T}} \\ -\left({}^{D}_{u_i}\boldsymbol{R}\right)_{:,3}^{\mathrm{T}} \end{bmatrix}, \tag{19}$$

$$\boldsymbol{J}_{\mathrm{fu}} = \begin{bmatrix} -\dfrac{1}{l_1}\left({}^{d_1}_{U}\boldsymbol{R}\right)_{:,2}\left(\boldsymbol{\omega}_{\mathrm{u}} \times {}^{U}_{D}\boldsymbol{R}\boldsymbol{u}_1^{\{U\}}\right)^{\mathrm{T}} - \left({}^{D}_{u_i}\boldsymbol{R}\right)_{:,1}^{\mathrm{T}} \\ -\dfrac{1}{l_2}\left({}^{d_1}_{U}\boldsymbol{R}\right)_{:,2}\left(\boldsymbol{\omega}_{\mathrm{u}} \times {}^{U}_{D}\boldsymbol{R}\boldsymbol{u}_1^{\{U\}}\right)^{\mathrm{T}} - \left({}^{D}_{u_i}\boldsymbol{R}\right)_{:,1}^{\mathrm{T}} \\ -\dfrac{1}{l_3}\left({}^{d_1}_{U}\boldsymbol{R}\right)_{:,2}\left(\boldsymbol{\omega}_{\mathrm{u}} \times {}^{U}_{D}\boldsymbol{R}\boldsymbol{u}_1^{\{U\}}\right)^{\mathrm{T}} - \left({}^{D}_{u_i}\boldsymbol{R}\right)_{:,1}^{\mathrm{T}} \end{bmatrix}, \tag{20}$$

$$\boldsymbol{J}_{\mathrm{xu}} = \begin{bmatrix} -\dfrac{1}{l_1}\left({}^{d_1}_{U}\boldsymbol{R}\right)_{:,1}\left(\boldsymbol{\omega}_{\mathrm{u}} \times {}^{U}_{D}\boldsymbol{R}\boldsymbol{u}_1^{\{U\}}\right)^{\mathrm{T}} - \left({}^{D}_{u_i}\boldsymbol{R}\right)_{:,2}^{\mathrm{T}} \\ -\dfrac{1}{l_2}\left({}^{d_1}_{U}\boldsymbol{R}\right)_{:,1}\left(\boldsymbol{\omega}_{\mathrm{u}} \times {}^{U}_{D}\boldsymbol{R}\boldsymbol{u}_1^{\{U\}}\right)^{\mathrm{T}} - \left({}^{D}_{u_i}\boldsymbol{R}\right)_{:,2}^{\mathrm{T}} \\ -\dfrac{1}{l_3}\left({}^{d_1}_{U}\boldsymbol{R}\right)_{:,1}\left(\boldsymbol{\omega}_{\mathrm{u}} \times {}^{U}_{D}\boldsymbol{R}\boldsymbol{u}_1^{\{U\}}\right)^{\mathrm{T}} - \left({}^{D}_{u_i}\boldsymbol{R}\right)_{:,2}^{\mathrm{T}} \end{bmatrix}, \tag{21}$$

Solving the first derivative of time of Eq. (3), the result is shown as follows:

$$\dot{\boldsymbol{p}}_{gi}^{\{d_i\}} = q_i\left(\boldsymbol{\omega}_{\mathrm{z}}^{\{d_i\}} \times \boldsymbol{e}_i\right) = q_i\begin{pmatrix}\dot{\phi}_{\mathrm{d}i} & \dot{\theta}_{\mathrm{d}i} & 0\end{pmatrix}^{\mathrm{T}}, \tag{22}$$

Combining Eq. (13) and Eq. (22), the Jacobian matrix of the lower connecting rod is:

$$\boldsymbol{J}_{gi} = \begin{bmatrix} \dfrac{q_i}{l_i}\left(\left(\boldsymbol{\omega}_{\mathrm{u}} \times {}^{U}_{D}\boldsymbol{R}\boldsymbol{u}_i^{\{U\}}\right)\left({}^{d_i}_{U}\boldsymbol{R}\right)_{:,2}\right)^{\mathrm{T}} \\ -\dfrac{q_i}{l_i}\left(\left(\boldsymbol{\omega}_{\mathrm{u}} \times {}^{U}_{D}\boldsymbol{R}\boldsymbol{u}_i^{\{U\}}\right)\left({}^{d_i}_{U}\boldsymbol{R}\right)_{:,1}\right)^{\mathrm{T}} \\ \boldsymbol{0}^{1\times 3} \end{bmatrix}, \tag{23}$$

Similarly, the Jacobian matrix of the upper connecting rod is:

$$\boldsymbol{J}_{\mathrm{h}i}=\begin{bmatrix}\dfrac{h_i}{l_i}\left(\left(\boldsymbol{\omega}_{\mathrm{u}}\times{}^{U}_{D}\boldsymbol{R}\boldsymbol{u}_i^{\{U\}}\right)\left({}^{d_i}_{U}\boldsymbol{R}\right)_{:,2}\right)^{\mathrm{T}}\\ -\dfrac{h_i}{l_i}\left(\left(\boldsymbol{\omega}_{\mathrm{u}}\times{}^{U}_{D}\boldsymbol{R}\boldsymbol{u}_i^{\{U\}}\right)\left({}^{d_i}_{U}\boldsymbol{R}\right)_{:,1}\right)^{\mathrm{T}}\\ \boldsymbol{0}^{1\times3}\end{bmatrix},\tag{24}$$

Where h_i is the distance between the centroid of the lower connecting rod and the center of the universal joint.

2.3 Dynamic Equation of Electro-hydraulic Driven 3-UPS/S Parallel Stabilized Platform

To derive the dynamic equation of electro-hydraulic drive 3-UPS/S parallel stabilized platform, the following assumptions need to be made:

(1) The errors in the process of processing and assembly are ignored;

(2) The force of the drive chain on the moving platform can be equivalent to the spring force along the expansion direction of the drive chain;

(3) The relative friction between components is ignored.

According to virtual work principle, the virtual power acting on each component of the mechanism is calculated as:

$$\begin{aligned}\delta p=&\left(\boldsymbol{f}_{\mathrm{u}}-\boldsymbol{k}\Delta\boldsymbol{l}-\boldsymbol{c}\dot{\boldsymbol{l}}\right)\square\delta\boldsymbol{l}+\left(-\boldsymbol{I}_{\mathrm{u}}\dot{\boldsymbol{\omega}}_{\mathrm{u}}-\boldsymbol{\omega}_{\mathrm{u}}\times\boldsymbol{I}_{\mathrm{u}}\boldsymbol{\omega}_{\mathrm{u}}\right)\square\delta\boldsymbol{\omega}_{\mathrm{u}}\\&+\left(-k_{\mathrm{xd}}\Delta\theta_{\mathrm{d}}\right)\square\delta\dot{\theta}_{\mathrm{d}}+\left(-k_{\mathrm{fd}}\Delta\psi_{\mathrm{d}}\right)\square\delta\dot{\psi}_{\mathrm{d}}+\left(-k_{\mathrm{xu}}\Delta\theta_{\mathrm{u}}\right)\square\delta\dot{\theta}_{\mathrm{u}}\\&+\sum_{i=1}^{3}\left(-m_{\mathrm{g}i}\ddot{\boldsymbol{p}}_{gi}^{\{di\}}\square\delta\dot{\boldsymbol{p}}_{gi}^{\{di\}}+\left(-\boldsymbol{I}_{gi}^{\{di\}}\dot{\boldsymbol{\omega}}_{gi}^{\{di\}}-\boldsymbol{\omega}_{gi}^{\{di\}}\times\boldsymbol{I}_{gi}^{\{di\}}\boldsymbol{\omega}_{gi}^{\{di\}}\right)\square\delta\boldsymbol{\omega}_{gi}^{\{di\}}\right),\\&+\sum_{i=1}^{3}\left(-m_{\mathrm{h}i}\ddot{\boldsymbol{p}}_{hi}^{\{di\}}\square\delta\dot{\boldsymbol{p}}_{hi}^{\{di\}}+\left(-\boldsymbol{I}_{hi}^{\{di\}}\dot{\boldsymbol{\omega}}_{hi}^{\{di\}}-\boldsymbol{\omega}_{hi}^{\{di\}}\times\boldsymbol{I}_{hi}^{\{di\}}\boldsymbol{\omega}_{hi}^{\{di\}}\right)\square\delta\boldsymbol{\omega}_{hi}^{\{di\}}\right)\\&+\left(-k_{\mathrm{fu}}\Delta\psi_{\mathrm{u}}\right)\square\delta\dot{\psi}_{\mathrm{u}}+\left(-k_{\mathrm{gu}}\Delta\gamma_{\mathrm{u}}\right)\square\delta\dot{\gamma}_{\mathrm{u}}=\boldsymbol{0}\end{aligned}\tag{25}$$

Where $\boldsymbol{f}_{\mathrm{u}}$ is the force matrix on the moving platform; $\boldsymbol{k}$ is the stiffness matrix of the drive chain; $\boldsymbol{c}$ is the damping matrix of the drive chain; $\boldsymbol{I}_{\mathrm{u}}$ is the inertia matrix of the moving platform; $\boldsymbol{\omega}_{\mathrm{u}}$ is the angular velocity of the moving platform; m_{gi} is the mass of the lower connecting rod; $\boldsymbol{p}_{gi}^{\{di\}}$ is the displacement vector of the lower connecting rod; $\boldsymbol{I}_{gi}^{\{di\}}$ is the inertia matrix of the lower connecting rod; $\boldsymbol{\omega}_{gi}^{\{di\}}$ is the angular velocity of the lower connecting rod; $m_{\mathrm{h}i}$ is the mass of the upper connecting rod; $\boldsymbol{p}_{hi}^{\{di\}}$ is the displacement vector of the upper connecting rod; $\boldsymbol{I}_{hi}^{\{di\}}$ is the inertia matrix of the upper connecting rod; $\boldsymbol{\omega}_{hi}^{\{di\}}$ is the angular velocity of the upper connecting rod.

Ignoring Coriolis force and centrifugal force, Eq. (25) can be simplified to:

$$\begin{aligned}&\left(\boldsymbol{f}_{\mathrm{u}}-\boldsymbol{k}\boldsymbol{J}_{\mathrm{u}}\boldsymbol{x}-\boldsymbol{c}\boldsymbol{J}_{\mathrm{u}}\dot{\boldsymbol{x}}\right)\delta\dot{\boldsymbol{x}}-\left(k_{\mathrm{xu}}\boldsymbol{J}_{\mathrm{xu}}\boldsymbol{x}\right)^{\mathrm{T}}\boldsymbol{J}_{\mathrm{xu}}\delta\dot{\boldsymbol{x}}\\&-\left(k_{\mathrm{xd}}\boldsymbol{J}_{\mathrm{xd}}\boldsymbol{x}\right)^{\mathrm{T}}\boldsymbol{J}_{\mathrm{xd}}\delta\dot{\boldsymbol{x}}-\left(k_{\mathrm{fd}}\boldsymbol{J}_{\mathrm{fd}}\boldsymbol{x}\right)^{\mathrm{T}}\boldsymbol{J}_{\mathrm{fd}}\delta\dot{\boldsymbol{x}}\\&-\left(k_{\mathrm{fu}}\boldsymbol{J}_{\mathrm{fu}}\boldsymbol{x}\right)^{\mathrm{T}}\boldsymbol{J}_{\mathrm{fu}}\delta\dot{\boldsymbol{x}}-\left(k_{\mathrm{gu}}\boldsymbol{J}_{\mathrm{gu}}\boldsymbol{x}\right)^{\mathrm{T}}\boldsymbol{J}_{\mathrm{gu}}\delta\dot{\boldsymbol{x}}\\&-\sum_{i=1}^{3}\left(\boldsymbol{I}_{gi}\boldsymbol{\omega}_{gi}\boldsymbol{J}_{gi}+\boldsymbol{I}_{hi}\boldsymbol{\omega}_{\mathrm{h}i}\boldsymbol{J}_{\mathrm{h}i}\right)\delta\dot{\boldsymbol{x}}=\boldsymbol{0}\end{aligned},\tag{26}$$

Where $\dot{\boldsymbol{x}}=\boldsymbol{\omega}_{\mathrm{u}}^{\mathrm{T}}$.

The components of $\boldsymbol{\omega}_{\mathrm{u}}$ are independent because the generalized coordinates are independent. Thus, the coefficients should all equal to 0. The explicit dynamic equation of the mechanism can be obtained as follows:

$$\boldsymbol{M}\ddot{\boldsymbol{x}}+\boldsymbol{C}\dot{\boldsymbol{x}}+\boldsymbol{K}\boldsymbol{x}=\boldsymbol{0},\tag{27}$$

Where

$$\boldsymbol{M}=\boldsymbol{I}_{\mathrm{u}}+\sum_{i=1}^{3}\left(\boldsymbol{J}_{gi}^{\mathrm{T}}\boldsymbol{I}_{gi}\boldsymbol{J}_{gi}+\boldsymbol{J}_{hi}^{\mathrm{T}}\boldsymbol{I}_{\mathrm{h}i}\boldsymbol{J}_{\mathrm{h}i}\right),\tag{28}$$

$$\boldsymbol{C}=\boldsymbol{J}_{\mathrm{u}}{}^{\mathrm{T}}\boldsymbol{c}\boldsymbol{J}_{\mathrm{u}},\tag{29}$$

$$\begin{aligned}\boldsymbol{K}=&\boldsymbol{J}_{\mathrm{u}}{}^{\mathrm{T}}\boldsymbol{k}\boldsymbol{J}_{\mathrm{u}}+\boldsymbol{J}_{\theta\mathrm{d}}{}^{\mathrm{T}}\boldsymbol{k}_{\theta\mathrm{d}}\boldsymbol{J}_{\theta\mathrm{d}}+\boldsymbol{J}_{\psi\mathrm{d}}{}^{\mathrm{T}}\boldsymbol{k}_{\psi\mathrm{d}}\boldsymbol{J}_{\psi\mathrm{d}}\\&+\boldsymbol{J}_{\theta\mathrm{u}}{}^{\mathrm{T}}\boldsymbol{k}_{\theta\mathrm{u}}\boldsymbol{J}_{\theta\mathrm{u}}+\boldsymbol{J}_{\psi\mathrm{u}}{}^{\mathrm{T}}\boldsymbol{k}_{\psi\mathrm{u}}\boldsymbol{J}_{\psi\mathrm{u}}+\boldsymbol{J}_{\gamma\mathrm{u}}{}^{\mathrm{T}}\boldsymbol{k}_{\gamma\mathrm{u}}\boldsymbol{J}_{\gamma\mathrm{u}}\end{aligned},\tag{30}$$

3 Free Vibration Analysis of Electro-Hydraulic Driven 3-UPS/S Parallel Stabilized Platform

3.1 Modal Analysis of Electro-Hydraulic Driven 3-UPS/S Parallel Stabilized Platform in Fixed Posture

The structure parameters of Electro-hydraulic drive 3-UPS/S parallel stabilized platform are shown in Table 1.

Table 1 Structure parameters of Electro-hydraulic driven 3-UPS/S parallel stabilized platform

Parameter Name	Parameter Value
Rotational inertia of the moving platform $\boldsymbol{I}_{\mathrm{u}}$ (kg · m^2)	diag[3.74 3.76 7.72]
Rotational inertia of the lower connecting rod $\boldsymbol{I}_{\mathrm{g}}$ (kg · m^2)	diag[0.96 0.96 0.0506]

Rotational inertia of the upper connecting rod $\boldsymbol{I}_h$ (kg · m^2)	diag[0.19 0.19 0.0069]
Radius of the moving platform r_u (m)	0.38
Radius of the static platform platform r_d (m)	0.51
Mass of the moving platform m_u (kg)	65.703
Mass of the lower connecting rod m_g (kg)	20.604
Mass of the upper connecting rod m_h (kg)	4.263
Piston diameter of the hydraulic cylinder d_1 (m)	0.04
Piston rod diameter of the hydraulic cylinder d_2 (m)	0.025
bulk modulus of oil E (Pa)	1180×10^{-6}
Oil density ρ (kg/m^3)	900
Stiffness value of universal joint in rotation direction around axis x_{di} k_{xd} (Nm/rad)	72.07
Stiffness value of universal joint in rotation direction around axis x_{di} k_{yd} (Nm/rad)	72.07
Stiffness value of spherical hinge in rotation direction around axis x_{ui} k_{xu} (Nm/rad)	51.15
Stiffness value of spherical hinge in rotation direction around axis y_{ui} k_{fu} (Nm/rad)	62.79
Stiffness value of spherical hinge in rotation direction around axis z_{ui} k_{gu} (Nm/rad)	64
viscous damping coefficient c N·(m/s)	1620

Based on the parameters shown in Table1, the modal and natural frequencies of the platform in the initial position α=0°, β=0°, γ=28° and the random position α=10°, β=10°, γ=28° are calculated, the results are shown in Table 2 and Table 3.

Table 2 Natural frequency and vibration mode at initial position

Order of natural frequency	first order natural frequency	Second order natural frequency	Third order natural frequency
Natural frequency value (Hz)	26.38	128.55	128.91
Main vibration modes	0	0.0278	-1
	-0.0001	-1	-0.0278
	1	-0.0007	0

Table 3 Natural frequency and vibration mode at random position

Order of natural frequency	first order natural frequency	Second order natural frequency	Third order natural frequency
Natural frequency value (Hz)	27.46	120.94	148.82
Main vibration modes	0.0678	-0.2417	-1
	0.0875	-1	0.2424
	1	0.0498	0.0234

After analyzing the data in Table 2 and Table 3, the following conclusions can be drawn:

(1) At the initial position, the natural frequency of deflection direction is the minimum, and the natural frequencies in the direction of rotation and pitch are approximately equal;

(2) There is a certain coupling relationship between the vibration response of pitching and rotation direction, but the coupling relationship between them and the deflection direction is small;

(3) With the position changing of the mechanism, the coupling of the vibration response in every direction is enhanced, and the natural frequencies of each order also change. This is because the Jacobian matrix of the mechanism changes, and affects the mass matrix and stiffness matrix of the mechanism;

(4) When the position of the mechanism changes, the natural frequencies of each order change differently. The first and third order natural frequencies increased, while the second order natural frequencies decreased;

(5) When the vibration frequencies are the first order, second order and third order natural frequencies respectively, the maximum vibration response appears in the deflection, pitching and rotation direction in turn. In actual working conditions, the external excitation frequency is most likely to approach the first order natural frequency, so the mechanism is most prone to vibration in the deflection direction.

3.2 Natural Frequency Analysis in Workspace of Electro-hydraulic Driven 3-UPS/S Parallel Stabilized Platform

When the platform is used to maintain the stability of the horizontal direction of the equipment, the change range of deflection angle is small, and the angle compensation is mainly carried out through the change of rotation and pitching direction. According to the workspace search theory, when deflection angle is 28°, The change range of pitch angle and rotating angle is the largest. Therefore, taking this position as the initial workspace, the natural frequency variation curve of the mechanism can be obtained as follows:

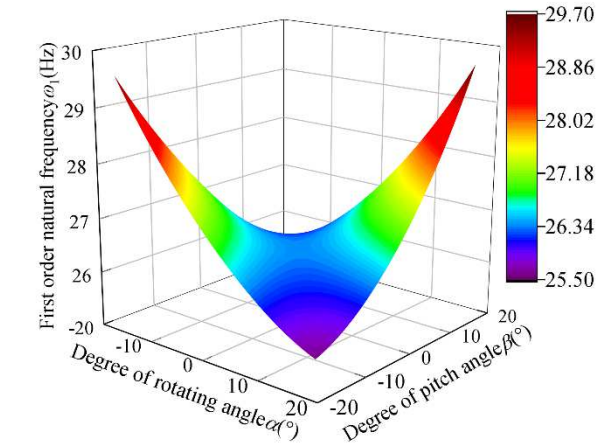

a) Variation law of first order natural frequency

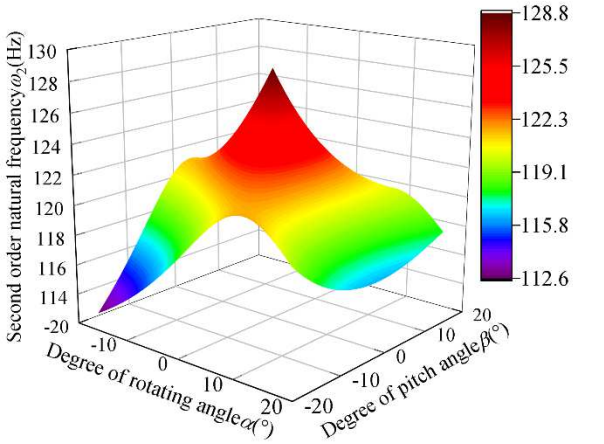

b) Variation law of second order natural frequency

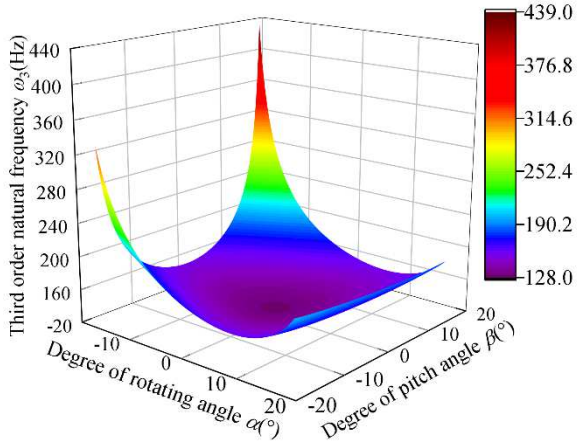

c) Variation law of third order natural frequency

Figure 2 Variation law of natural frequency in initial workspace

It can be seen from Figure 2 that in the initial workspace, natural frequencies of each order present obvious symmetry with position changing, and the first order natural frequency is the most obvious, corresponding to the movement in the deflection direction. When the mechanism gradually deviates from the initial position, the variation trend of each order natural frequency is not the same. Meanwhile, the positions where the maximum and minimum values of each order natural frequency are obtained are different. In general, when the pitching angle is quite different from the rotating angle, the natural frequency will approach the limit value. However, the second order natural frequency has a large value near the initial position. When the mechanism gradually deviates from the initial position through attitude compensation, the second order natural frequency decreases gradually. In addition, the third order natural frequency is most sensitive to position change, followed by the second order natural frequency, and the first order natural frequency is least affected by position change.

4 Force Vibration Analysis of Electro-Hydraulic Driven 3-UPS/S Parallel Stabilized Platform

4.1 Vibration Response Analysis of Electro-hydraulic Driven 3-UPS/S Parallel Stabilized Platform

When the excitation frequency is close to natural frequency of each order, the mechanism will generate resonance, which will affect the compensation accuracy and control accuracy. Therefore, when the structural parameters remain unchanged, the vibration response of the mechanism at the random position α=10°, β=10°, γ=28° is solved. The torque matrix acting on the mechanism is as follows:

$$\boldsymbol{M}_{\mathrm{U}}=\begin{bmatrix}80\cos(\omega_0 t)\\80\cos(\omega_0 t)\\80\cos(\omega_0 t)\end{bmatrix} \tag{31}$$

The time domain curve of vibration response is shown in Figure 3. As can be seen from the Figure 3, When subjected to an external harmonic excitation whose frequency is close to the natural frequency, the mechanism will generate resonance, and the steady state response is simple harmonic motion. When the excitation frequency is close to the first, second and third order natural frequency, the angular displacement in deflection, pitch and rotation direction reaches the maximum respectively. Meanwhile, when the external excitation frequency is close to the first order natural frequency, the angular displacement of the mechanism in rotation direction and pitching direction is approximately equal, but when the angular displacement in rotation direction or pitching direction reaches the maximum, the angular displacement response in the other two directions is smaller, which is consistent with the main vibration mode.

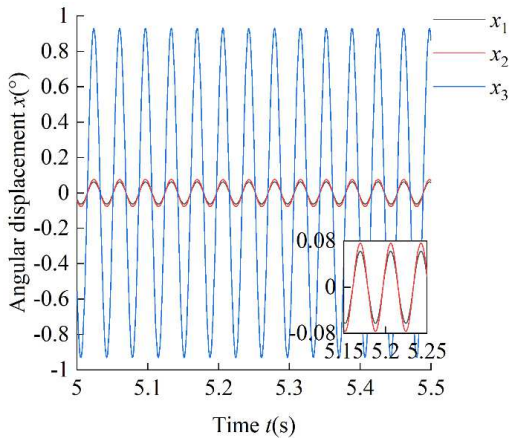

a) Time domain response when $\omega_0 \approx \omega_1$

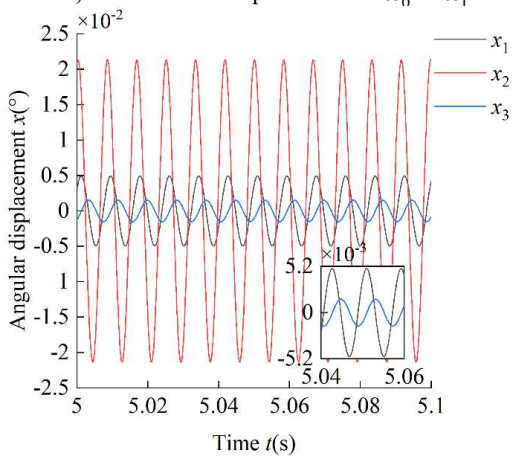

b) Time domain response when $\omega_0 \approx \omega_2$

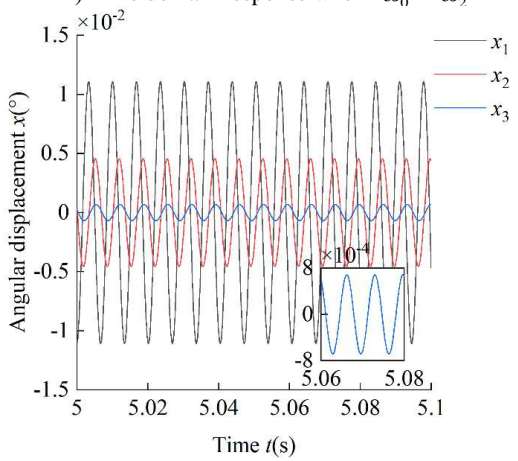

c) Time domain response when $\omega_0 \approx \omega_3$

Figure 3 Time domain curve of forced vibration

The frequency domain response curve of vibration response is shown in Figure 4. It can be seen that when the excitation frequency is close to each order natural frequency the steady-state vibration response amplitude in each direction reaches the maximum at the corresponding natural frequency. The maximum amplitude of vibration response is 0.932° in deflection direction, 0.0213° in pitching direction., and 0.0111° in rotation direction. Meanwhile, when the excitation frequency is close to the first, second and third order natural frequency, the steady-state response amplitude in each direction gradually decreases. When the excitation frequency is close to the first order natural frequency, the steady-state vibration response of in each direction is much larger than that when the excitation frequency is close to the second or third natural frequency. Thus, when the excitation frequency is close to the first order natural frequency, the resulting resonance will have a great influence on the compensation accuracy and control accuracy.

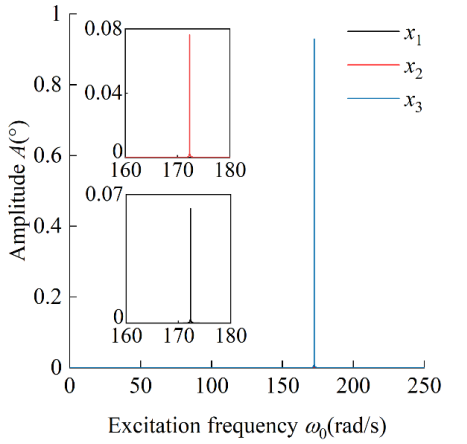

a) Frequency domain response when $\omega_0 \approx \omega_1$

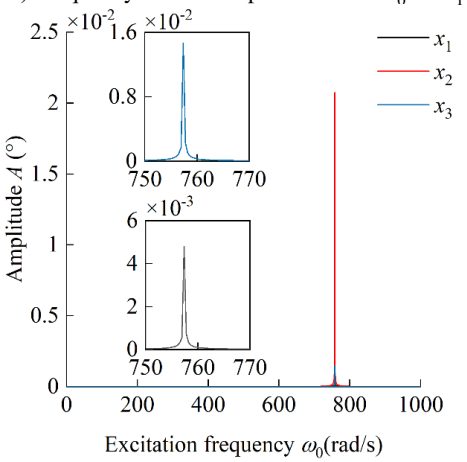

b) Frequency domain response when $\omega_0 \approx \omega_2$

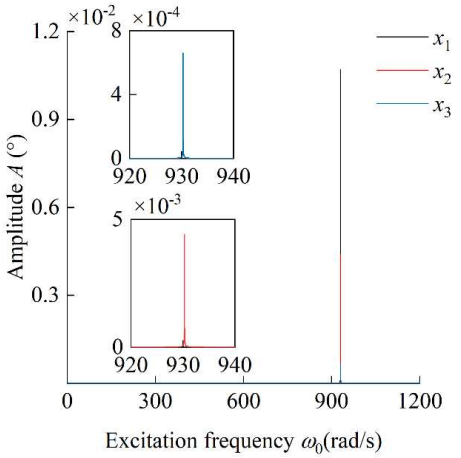

c) Frequency domain response when $\omega_0 \approx \omega_3$

Figure 4 Frequency domain curve of forced vibration

4.2 Vibration Response Amplitude Analysis in Workspace of Electro-hydraulic Driven 3-UPS/S Parallel Stabilized Platform

The amplitude of vibration response is also related to the position of the mechanism. Therefore, basing on keeping the theoretical parameters unchanged, the vibration response amplitude in the initial working space when the excitation frequency is close to the first order natural frequency is calculated, and the results are shown in Figure 5.

It can be seen from Figure 5 that when the excitation frequency is close to the first order natural frequency, the amplitude curves of vibration response in each direction show a certain symmetry, and the locations where the extreme values of response amplitudes in each direction are obtained are not the same. From Figure 5a), we can know that the vibration response amplitude in rotation direction is small when degree of pitch angle is near 0°. In this position, the vibration response amplitude in the rotation direction is insensitive to the position change in the pitching direction. Similarly, as can be seen from Figure 5b), the vibration response amplitude in the pitching direction is relatively small when degree of pitch angle is near 0°. In this position, the vibration response amplitude in pitching direction is insensitive to the position change in rotation direction. When the mechanism gradually deviates from the initial position, the amplitude of vibration response in the rotation and pitching directions increases gradually. When the difference between the rotation angle and the pitch angle is large, the vibration response amplitude in rotation direction and pitching direction is large. As can be seen from Figure 5c), when the position changes from the left limit to the right limit of the working space, the amplitude of the vibration response in the deflection direction increases gradually. And when the excitation frequency is close to the first natural frequency, the vibration response amplitude in the deflection direction is much larger than that in the pitch and rotation directions, and the maximum value is more than 1°. The vibration generated by the mechanism will have a great impact on the control accuracy.

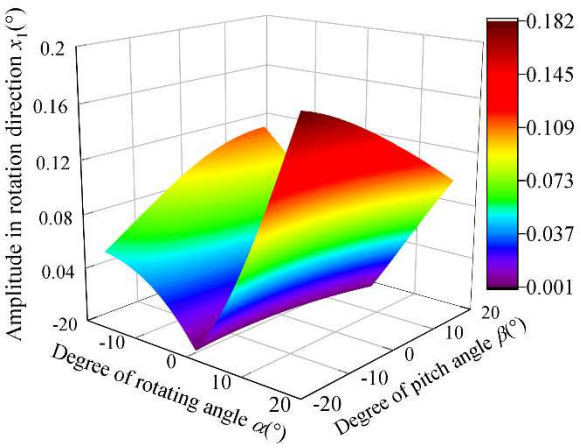

a) Amplitude of vibration response in rotation direction

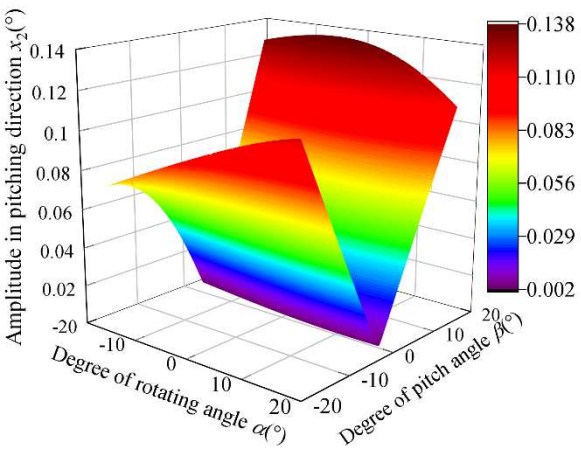

b) Amplitude of vibration response in pitching direction

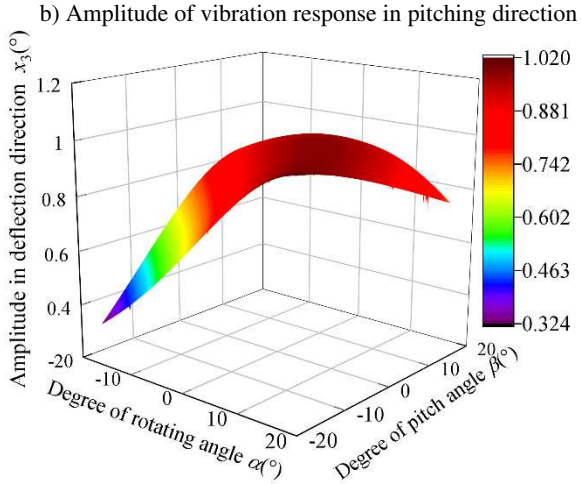

c) Amplitude of vibration response in deflection direction

Figure 5 Amplitude of vibration response when $\omega_0 \approx \omega_1$

5 Verification of Dynamic Theoretical Model of Electro-hydraulic Driven 3-UPS/S Parallel Stabilized Platform

5.1 Verification of Free Vibration Theoretical Model

To verify the correctness of free vibration theoretical model, the natural frequency of the prototype at random position α=10°, β=10°, γ=28° is measured by using pulse excitation method. The experimental schematic diagram is shown in Figure 6. The force hammer strikes the moving platform to generate impulse excitation force. Then, the signal of the exciting force enters the lower computer through the force sensor and voltage amplifier on the force hammer, and the axial response signal of the prototype is collected by the acceleration sensor and input to the computer through the voltage amplifier and the lower computer.

The sampling frequency used in the experiment is 640Hz, so it meets the sampling theorem and the collected signals are reliable. The time-domain curves of excitation signals and vibration signals collected in the experiment are shown in Figure 9.

After processing the data obtained in Figure 9, the power spectral density curve of the prototype response signal can be obtained, as shown in Figure 10. The curve has peaks at 26.31Hz, 126.41Hz and 141.88Hz. Compared with the theoretical value of the natural frequency, the maximum error between the theoretical value and the experimental value is 4.66%, which can verify the correctness of the theoretical model.

Table 4 Comparison of theoretical and experimental values of natural frequency

Experimental result	Theoretical value/(Hz)	Experimental value/(Hz)	error/(%)
First order natural frequency	27.46	26.31	4.18
Second order natural frequency	120.94	126.41	4.5
Third order natural frequency	148.82	141.88	4.66

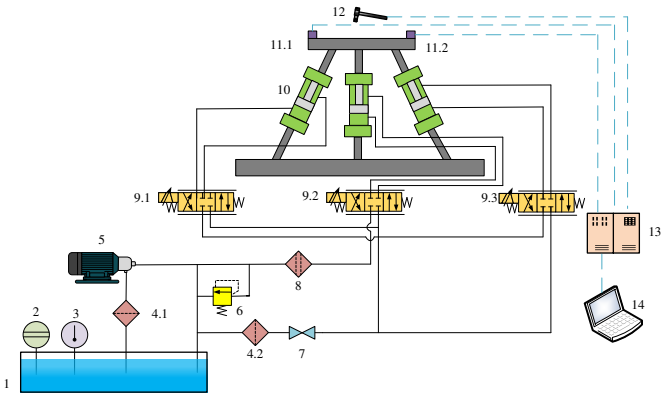

1 Oil tank 2 Liquid level gauge 3 Liquid temperature gauge 4 filter 5 Motor pump 6 Overflow valve 7 Check valve 8 Filter 9 Servo valve 10 Electro-hydraulic drive 3-UPS/S parallel stabilized platform prototype 11 Acceleration sensor 12 Force hammer 13 Lower computer 14 Computer

Figure 6 Schematic diagram of modal experiment

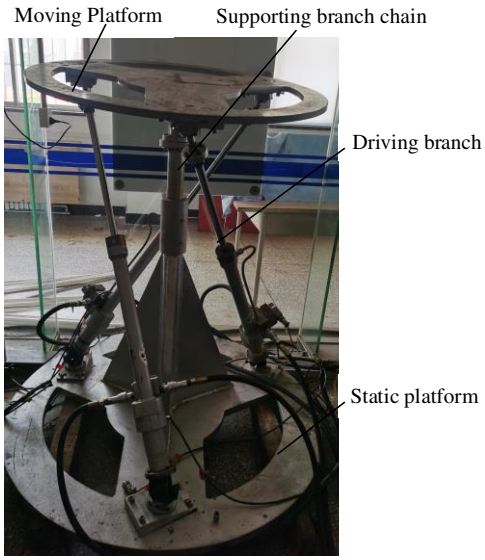

Figure 7 Electro-hydraulic drive 3-UPS/S parallel stabilized platform prototype

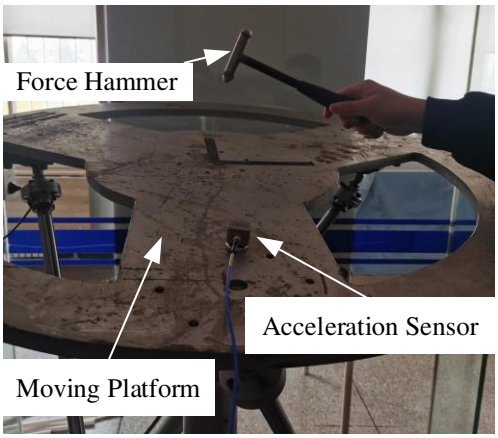

a) Modal test platform

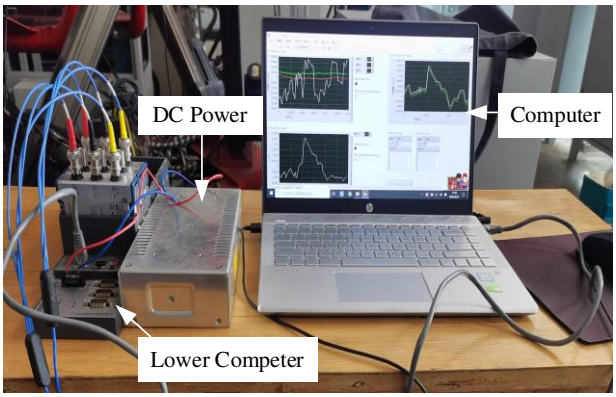

b) Signal acquisition and analysis system

Figure 8 Modal test diagram

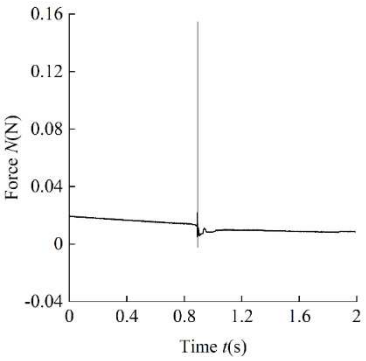

a) Excitation signal of the system

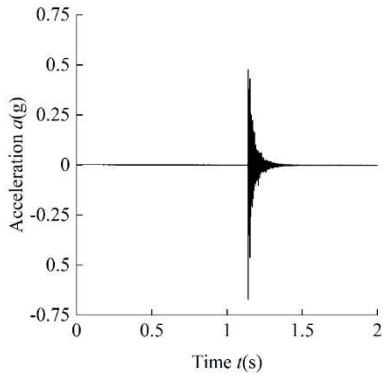

b) Acceleration response of the system

Figure 9 Time domain curve of measured signal

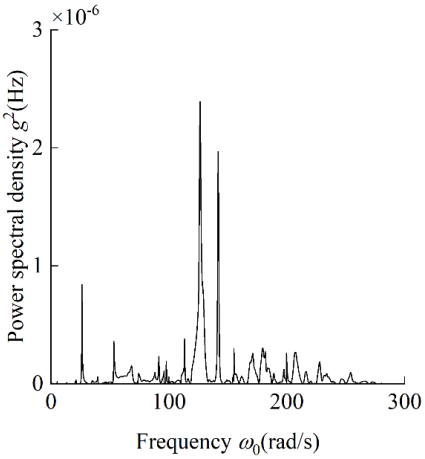

Figure 10 The power spectral density of the system response

5.2 Verification of Forced Vibration Theoretical Model

To verify the correctness of the forced vibration theoretical model of the mechanism, taking the excitation frequency close to the first order natural frequency as example, the fourth-order Runge-Kutta method is used to solve the time-domain and frequent-domain characteristic curves of the vibration response, and the results are shown in Figure 11.

As can be seen from Figure 11a), when the excitation frequency is close to the first order natural frequency, the time-domain curve of the numerical solution presents stable simple harmonic motion, which is consistent with the results of theoretical analysis. By comparing Figure 3b) and Figure 11b), it can be seen that the numerical solutions of the maximum vibration response amplitude in the rotation, pitching and deflection directions are 0.0627°, 0.0766° and 0.932° respectively. Correspondingly, the maximum vibration response amplitude obtained by theoretical calculation in each direction is 0.0626°, 0.0765° and 0.9316° respectively. The maximum error between the theoretical solution and the numerical solution is 0.016%, which can verify the correctness of the forced vibration theoretical

model.

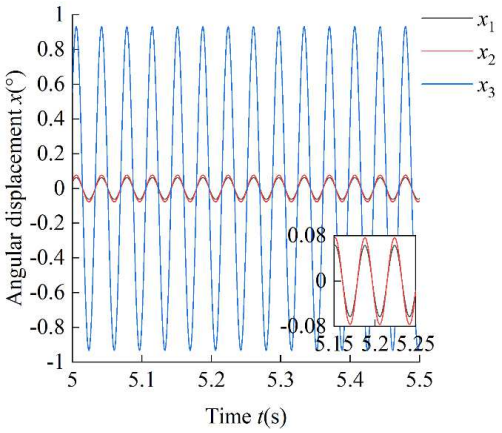

a) Time domain curve of numerical solution

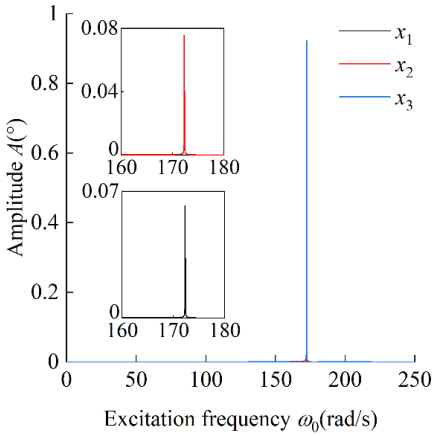

b) Frequency domain curve of numerical solution

Figure 11 Time domain curve of steady-state response numerical solution

Table 5 Comparison of theoretical and numerical values of maximum vibration response amplitude

Direction	Theoretical value/(°)	Numerical value/(°)	error/(%)
Rotation direction	0.0627	0.0626	0.16
Pitching direction	0.0766	0.0765	0.13
Deflection direction	0.932	0.9316	0.042

6 Conclusions

(1) The natural frequency is a function of the position of the mechanism. In the initial working space, the change of the natural frequency is symmetrical, and the position of obtaining the extreme value is not the same. With the change of position, the third order natural frequency changes most sharply, followed by the second order natural frequency, and the first order natural frequency changes most gently;

(2) When the mechanism is resonated by the external excitation of simple harmonic motion, the steady-state resonance response presents simple harmonic motion. When the excitation frequency is close to the first, second and third order natural frequency, the amplitude of the vibration response reaches the maximum in the direction of deflection, pitching and rotation respectively;

(3) The vibration response amplitude varies symmetrically in the initial working space. When the excitation frequency is close to the first natural frequency, the vibration response amplitude in the deflection direction is larger than that in the other two directions, and the value is close to 1°, which will have a great influence on the compensation accuracy and control accuracy;

(4) The modal test and fourth-order Runge-Kutta numerical simulation method are used to verify the theoretical model. The maximum error between the theoretical value and the experimental value is 4.66%, and the maximum error between the numerical value and the theoretical value values 0.016%, which verifies the correctness of the theoretical model m.

Authors' Contributions

Xiaoming Yuan and Lijie Zhang were in charge of the whole trial; Weiqi Wang wrote the manuscript; Haodong Pang assisted with sampling and laboratory analyses. All authors read and approved the final manuscript.

Author Details

[1] Hebei Key Laboratory of Heavy Machinery Fluid Power Transmission and Control,Yanshan University, Qinhuangdao,066004. [2] Key Laboratory of Advanced Forging & Stamping Technology and Science, Ministry of Education, Yanshan University,Qinhuangdao,066004

Authors' Information

Xiaoming Yuan, born in 1984, is currently an associate professor at *Yanshan University, China*. He received his Ph.D. degree from *Yanshan University, Qinhuangdao, China*, in 2014. His research interests include fluid-structure interaction dynamics of fire-fighting monitor, fluid transmission and control, and new magnetic gear transmission and control. Tel: +86-13780560557; E-mail: xiaomingbingbing@163.com

Weiqi Wang, received the B.S. degree from the School of Mechanical Engineering, Yanshan University, China, in 2020, where he is currently pursuing the master's degree. His research interests include fluid transmission and control. E-mail: wang0505204@163.com

Haodong Pang, born in 1998, received the B.S. degr ee from the School of Mechanical Engineering, *Nanjin g Normal University Zhongbei College*, China in 2020.

He is currently pursuing the master's degree in *Yansh -an University*. His research interests include fluid and electromagnetic transmission. E-mail: pang_haodong@163.com

Lijie Zhang, born in 1969, is currently the vice-president at *Hebei Agricultural University, China*. He received his Ph.D. degree from *Yanshan University, China*, in 2006. His research interests include reliability and fault diagnosis of hydraulic components, multiphysics coupling analysis, and mechanics and robotics. E-mail: ljzhang@ysu.edu.cn

Competing Interests

The authors declare no competing financial interests.

Acknowledgements

Not applicable.

Funding

Supported by National key research and development program (Grant number: 2019YFB2005303), General Fund of National Natural Science Foundation of China (Grant number: 52175066), Hebei Natural Science Foundation (No. E2020203090) and Key Science and Technology Projects in Colleges and Universities of Hebei Province (No. ZD2022052).

References

[1] Y C Wang, Y M Yang, H P Kuang. High performance both in low-speed tracking and large-angle swing scanning based on adaptive nonsingular fast terminal sliding mode control for a three-axis universal inertially stabilized platform. *Sensors*, 2020, 20(20): 16-18.

[2] X Y Zhou, Y Jia, Y Li Y. An integral sliding mode controller based disturbances rejection compound scheme for inertially stabilized platform in aerial remote sensing. *Proceedings of the Institution of Mechanical Engineers*, 2018, 232(5): 26-27.

[3] A Papanikolaou, G Zaraphonitis. Computer-aided simulations of large amplitude roll motions of ships in waves and of dynamic stability. *IOS Press*, 1987, 34(399): 170-211.

[4] M Y Zhang, Y L Guan, W W Zhao. Adaptive super-twisting sliding mode control for stabilization platform of laser seeker based on extended state observer. *Optik*, 2019, 12(33): 199-201.

[5] J M Hilkert. Inertially stabilized platform technology concepts and principles. *IEEE Control Systems Magazine*, 2008, 28(1): 26-46.

[6] L L Wang, J Z Xiao, H Wang, et al. Development of a parallel-series stabilized platform system. *Applied Mechanics and Materials*, 2013, 319: 414-418.

[7] F Dong, X S Lei, W S Chou. A Dynamic Model and Control Method for a Two-Axis Inertially Stabilized Platform. I*EEE Transactions on Industrial Electronics*, 2017, 64(1): 432-439.

[8] M Latifinavid, A Azizi. Kinematic modelling and position control of a 3-DOF parallel stabilizing robot manipulator. *Journal of Intelligent & Robotic Systems*, 2013, 107(2): 17.

[9] A Morinaga, T Ogawa, K Iwanaga, et al. Development of motion reduction device for ship using underactuated parallel link mechanism. *Sensors and materials: An International Journal on Sensor Technology*, 2021, 33(3): 897-906.

[10] W J Liu, J L Du, J Li, et al. Stabilization control of 3-DOF parallel vessel-borne platform with dynamic uncertainties and unknown disturbances. *Applied Ocean Research*, 2022, 126(21): 1-11.

[11] W Hunek, P Majewski, J Zygarlicki, et al. A measurement-aided control system for stabilization of the real-life stewart platform. *Sensors* ,2022, 22(19): 7271.

[12] H J Hong, X Y Zhou, Z Y Zhang, et al. Modeling and calibration of pointing errors using a semi-parametric regression method with applications in inertially stabilized platforms. *New Astronomy*, 2016, 47:105-110.

[13] X M Yuan, W Q Wang, X Zhu, et al. Analysis of free vibration of hydraulic opposing cylinder controlled by servo valve. *Transactions of the Canadian Society for Mechanical Engineering*, 46: 651-667.

[14] X M Yuan, W Q Wang, X Zhu, et al. Analysis of parametric vibration of hydraulic opposing cylinder controlled by servo valve considering pressure pulsation. *Transactions of the Canadian Society for Mechanical Engineering*, 2022, 46: 668-684.

[15] J R Gevinski, R Pederiva R. Prediction of dynamic strain using modal parameters. *Journal of the Brazilian Society of Mechanical Sciences and Engineering*, 2016, 38(1): 49-57.

[16] Z W Cao, G Yao G. Parametric vibration stability analysis of a pyramid lattice sandwich plate subjected to pulsatile external airflow. *Acta Mechinica Solida Sinica*, 2023, 36(1): 95-104.

[17] Y C Zhu, S K Au SK. Bayesian data driven model for uncertain modal properties identified from operational modal analysis. *Mechanical Systems and Signal Processing*, 2020, 136: 1-24.

[18] C O Zhi, C T Hong, A Brandt, et al. An inconsistent phase selection assessment for harmonic peaks elimination in operational modal testing. *Archive of Applied Mechanics*, 2019, 89(12): 2415-2430.

[19] J H Yang, H F Lam, L B James. Bayes-Mode-ID: A Bayesian modal-component-sampling method for operational modal analysis. *Engineering Structures*, 2019, 189: 222-240.

[20] H Chen, C H Lu, Z E Liu, et al. Structural modal analysis and optimization of SUV door based on response surface method. *Shock and Vibration*, 2020, 2020: 9362434.

[21] P G Golano, L Z Fragonara, P Morantz, et al. Numerical and experimental modal analysis applied to an optical test system designed for the form measurements of metre-scale optics. *Shock and Vibration*, 2018, 2018: 3435249.

[22] J H Roh, J H Woo I Lee. Thermal post-buckling and vibration analysis of composite conical shell structures using layerwise theory. *Journal of Thermal Stresses*, 2009, 32(1-2): 41-64.

[23] T Wang, O Celik, F N Catbas, et al. A frequency and spatial domain decomposition method for operational strain modal analysis and its application. *Engineering Structures*, 2016, 114(1): 104-112.

[24] I Zaghbani, V Songmene. Estimation of machine-tool dynamic parameters during machining operation through operational modal analysis. *International Journal of Machine Tools & Manufacture*, 2009, 49(12): 947-957.

[25] Z F Bin, Z C Ong, S Y Khoo. A review of operational modal analysis techniques for in-service modal identification. *Journal of the Brazilian Society of Mechanical Sciences and Engineering*, 2020, 42(8): 398.

[26] F Ebrahimi, E Salari E. Thermal buckling and free vibration analysis of size dependent Timoshenko FG nanobeams in thermal environments. *Composite Structures*, 2015, 128: 363-380.